Available online at www.CivileJournal.org

Civil Engineering Journal

(E-ISSN: 2476-3055; ISSN: 2676-6957)

Vol. 12, No. 04, April, 2026

Numerical Assessment of Integrated Perforated and Recurved Seawall Designs for Tsunami Mitigation

Weixiao Jiang [1], Wei Chek Moon [1*], Huanhuan Du [2], Tze Liang Lau [3],
How Tion Puay [4], Jin Chai Lee [1]

[1] *Department of Civil Engineering, Faculty of Engineering, Technology and Built Environment, UCSI University, Kuala Lumpur 56000, Malaysia.*

[2] *College of Architecture and Energy Engineering, Wenzhou University of Technology, Wenzhou 325000, China.*

[3] *School of Civil Engineering, Universiti Sains Malaysia, Nibong Tebal, Penang 14300, Malaysia.*

[4] *River Engineering and Urban Drainage Research Centre, Universiti Sains Malaysia, Nibong Tebal, Penang 14300, Malaysia.*

Received 10 January 2026; Revised 20 March 2026; Accepted 26 March 2026; Published 01 April 2026

Abstract

Tsunami wave overtopping remains a major challenge for conventional vertical seawalls. Alternative seawall designs have therefore been proposed to address the overtopping issue. This study aims to conduct a staged numerical investigation to evaluate the hydraulic performance of solid, perforated, and integrated perforated–recurved seawall configurations. Tsunami-like waves were simulated in a numerical flume at two impoundment depths under dry and wet bed conditions. The results reveal that perforation significantly reduced peak horizontal wave forces by about 25-30%, depending on the perforation ratio and wave conditions. Nevertheless, this force reduction led to an increase in overtopping discharge, along with higher inland flow depth and velocity. This demonstrates that wave energy is redistributed rather than eliminated. The subsequent multi-criteria performance evaluation found that a 20% perforation ratio offers an optimal compromise between hydraulic performance and material efficiency. Building on this configuration, two types of integrated perforated-recurved seawalls were tested, incorporating triangular and arc-recurved profiles. The results indicate that the addition of the recurved crest elements in the design improved overall energy dissipation from approximately 52% (perforated-only) to over 90% for near-threshold overtopping under dry bed conditions. Among the integrated design types, triangular recurved performed slightly better than arc types. Incorporating perforations and recurves partially offset the disadvantages of each design, and these results demonstrate that such a design is effective and adaptable for mitigating coastal flood risk and improving coastal resilience against tsunamis.

Keywords: Seawall; Wave Force; Overtopping Volume; Inland Depth and Velocity; Energy Dissipation.

1. Introduction

Tsunamis are often referred to as "harbor waves" due to their origin in the Japanese term, which was used to describe the first reported occurrence of disturbance waves in Japanese harbors. Tsunamis result from disturbances caused by underwater earthquakes, violent volcanic eruptions, or even landslides. Because of their very long wavelengths, tsunamis can travel across oceans at speeds up to 800 km/h before undergoing rapid shoaling amplification in shallow coastal waters [1]. This shoaling process results in a sudden rise in wave height and energy, which can cause catastrophic coastal inundation and destruction of infrastructure and loss of human life. In 2004, a tsunami struck the Indian Ocean, causing

---

* Corresponding author: vmoonpower@yahoo.com.my

https://doi.org/10.28991/CEJ-2026-012-04-01

over 227,000 deaths across several countries [2], while in 2011, the Great East Japan Earthquake triggered a tsunami that caused over 18,000 deaths and extensive damage to coastal defenses in different regions, including Miyako, where the seawalls were overtopped by the high waves [3].

Seawalls have been commonly used as the primary structures for coastal protection, as they dissipate wave energy and prevent inland wave propagation. However, various post-disaster investigations have revealed that seawalls have failed due to extreme loading from incoming waves and instabilities within the structure and the ground on which the seawalls are constructed [4, 5]. Therefore, failure of conventional seawalls was found to occur through various modes. Block-type structures require strong interlocking systems to prevent disintegration, while gravity seawalls, such as the failed Taro seawall, revealed the importance of mitigating overtopping and foundation scour [6]. The detachment of seawall plates during the 2018 Sulawesi tsunami also showed significant vertical uplift and downward pressure as part of the tsunami loading, in addition to horizontal forces [7]. These real-world failures suggest that tsunami loading is highly transient and involves coupled hydrodynamic and geotechnical processes that conventional seawall designs are unable to withstand.

In response to these challenges, several innovative seawall designs have been investigated in recent years. Perforated walls, which are built with openings, have gained considerable attention because the openings within the wall allow partial flow transmission. Experimental studies demonstrate that perforated seawalls are effective in controlling flow and dissipating energy, leading to decreased direct wave impact on the seawall [8, 9]. However, it has also been found that perforations may elevate flow transmission, which highlights a fundamental trade-off between structural protection and flood hazard mitigation [10]. Recent investigations, meanwhile, confirm that perforated structures can reduce hydrodynamic loads considerably but may increase the risk of inland inundation under certain wave conditions [11-13].

Another alternative seawall design involves curved and recurved types, which aim to redirect incident waves upward or seaward and minimize impact loads on landward structures. Notably, Gupta et al. [14] showed that curved seawalls offer a 30% reduction in impact forces compared to vertical designs, while Ravindar et al. [15] demonstrated that the seawall curvature has a significant effect on the impact pressure and force distribution along the wall face. Ghassemizadeh et al. further studied the interaction of isolated waves with different geometries of curved seawalls [16, 17]. The results indicate that curved seawall design is of considerable importance, as certain curved profiles can minimize reflection while simultaneously increasing surge elevation, indicating trade-offs in geometric modification.

In parallel, recurved seawalls are characterized by vertical seawalls fitted with a backward-curving crest or parapet that is specifically designed to reduce overtopping by deflecting uprushing water seaward [18]. The effectiveness of recurved designs was demonstrated by Harish et al. [19], who observed that large-recurve configurations are more effective for low-lying walls, as they can delay the timing of the impact and reduce the load on structures located inland. On the other hand, Benoit et al. [20] and de Almeida [21] further found that recurved elements significantly altered breaking-wave dynamics and caused localized pressure amplification near the crest and highly concentrated impact regions. In contrast to curved profiles, the recurved configurations can more evenly distribute the forces, which can lower the risk of cracking and structural failure under impulsive wave loads [22].

Despite these advances, several important knowledge gaps remain. Most existing studies evaluate seawall types independently, without considering the potential combined effects of perforations with geometric modifications. The underlying mechanisms, particularly the energy dissipation by perforations and flow redirection by recurved crests, have not been well documented. Previous investigations of curved and recurved walls also reported improved overtopping control but increased local structural loads. Therefore, the trade-off between force reduction and inland hazard remains insufficiently quantified. A comprehensive evaluation incorporating multiple performance metrics is therefore needed to inform optimal design.

To address these gaps, this study conducts a staged numerical investigation to evaluate the performance of solid, perforated, and integrated perforated-recurved seawalls in terms of forces, overtopping, inland inundation, and energy dissipation. Multiple perforation ratios are examined under both dry and wet bed tsunami conditions, and an optimized perforation design is subsequently combined with alternative recurved crest geometries to evaluate the integrated configurations. This staged approach allows the effects of perforations and crest modifications to be assessed independently and in combination, thereby providing insight into tsunami–seawall interaction, supporting the development of more resilient coastal protection strategies against tsunami hazards.

2. Research Methodology

A schematic flowchart summarizing the overall staged numerical methodology adopted in this study is shown in Figure 1. The workflow consists of two sequential stages, starting with perforation optimization, followed by integrated perforated-recurved configurations.

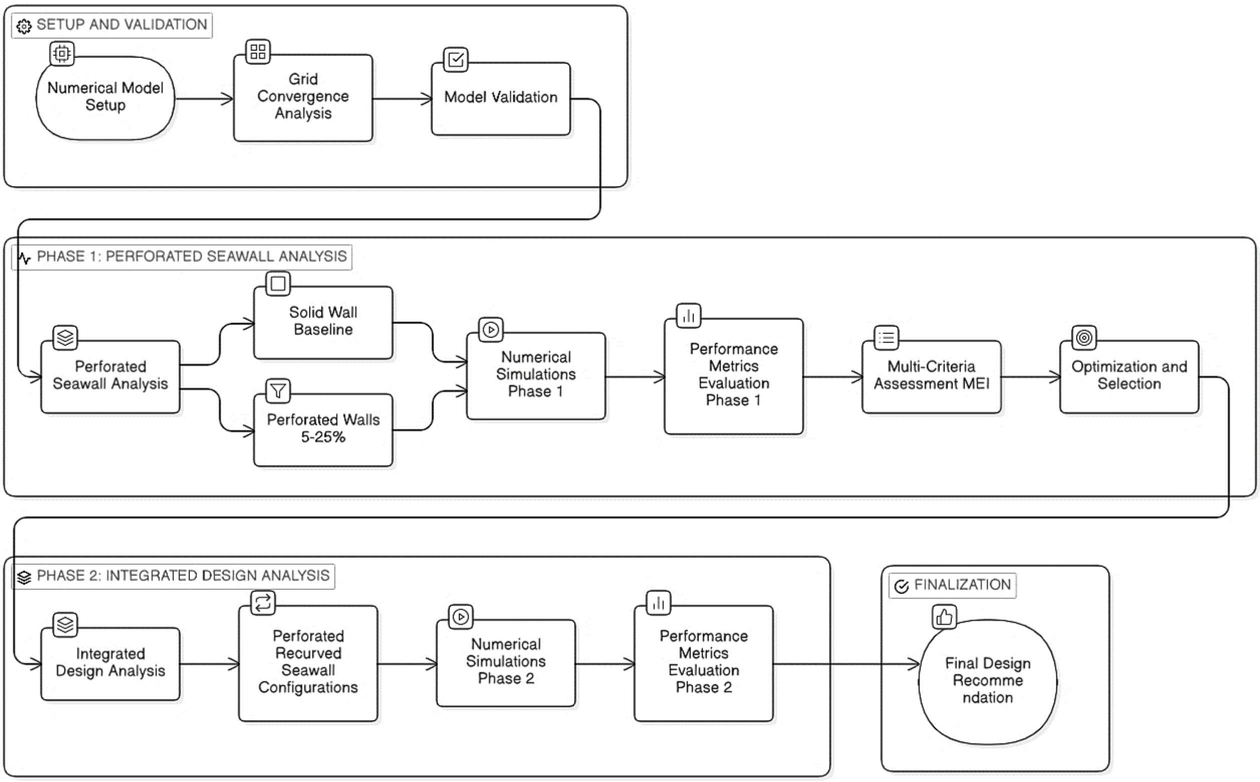

Figure 1. Flowchart of the staged numerical methodology for evaluating perforated and integrated perforated–recurved seawall designs under tsunami loading

2.1. Numerical Model Descriptions

This study employed the commercial computational fluid dynamics (CFD) software FLOW-3D, developed by Flow Science, Inc., to numerically simulate tsunami–structure interactions. FLOW-3D is widely used for transient free-surface flow problems, especially in hydraulic and coastal engineering applications. The governing equations solved in FLOW-3D consist of the continuity equation and the momentum equations for Newtonian, incompressible fluid flow, expressed as:

$$\frac{\partial}{\partial x_i}(u_i A_i) = 0 \tag{1}$$

$$\frac{\partial u_i}{\partial t} + \frac{1}{V_F}\left(u_j A_j \frac{\partial u_i}{\partial x_j}\right) = -\frac{1}{\rho}\frac{\partial p}{\partial x_i} + g_i + f_i \tag{2}$$

where, u_i and g_i are the velocity component and gravitational acceleration in the x_i direction (x, y, z); V_F is the fractional volume of fluid within each computational cell; A_j represents the fractional open area to flow in the respective coordinate directions; t denotes time; ρ is fluid density; p is pressure; and f_i is the stress term, which requires turbulence closure.

To simulate wave–structure interaction, the Reynolds-averaged Navier–Stokes (RANS) approach was adopted to capture the mean flow characteristics. The governing equations were discretized using the finite volume method on a structured Cartesian grid composed of hexahedral cells. Turbulence effects were modelled using the Renormalization Group (RNG) turbulence model k–ε proposed by Yakhot & Orszag [23], which has been shown to perform well under transitional and moderately turbulent flow conditions typical of wave impact problems.

Free-surface tracking was achieved using the Volume of Fluid (VOF) method originally developed by Hirt & Nichols [24]. In this approach, a volume fraction with a value between zero (empty) and one (fully filled) was assigned for each cell. To enhance numerical accuracy and stability, a second-order monotonicity-preserving advection scheme was applied for the transport equations. The rigid obstacle was set by using the Fractional Area/Volume Obstacle Representation (FAVOR) technique [25], which allows complex and irregular geometries to be accurately embedded within a structured Cartesian grid by partially blocking the computational cells.

2.2. Computational Setup

2.2.1. Numerical Wave Flume

For the numerical modelling, as shown in Figure 2, the simulations were conducted in a numerical flume with dimensions of 244 m in length and 15 m in width. A 117 m long water reservoir was connected at the upstream end of the flume. This reservoir-based configuration produced tsunami-like bore waves that matched those generated in the laboratory experiments. The seabed in front of the seawall had a 1:50 slope to replicate the coastal cross-sections commonly found along the coastline. The landward side had a horizontal plain that was 1.96 m above the base of the seawall to represent the protected hinterland area. This topographic configuration enabled a realistic overtopping assessment, providing a means to measure the depth and flow velocity of inland flooding.

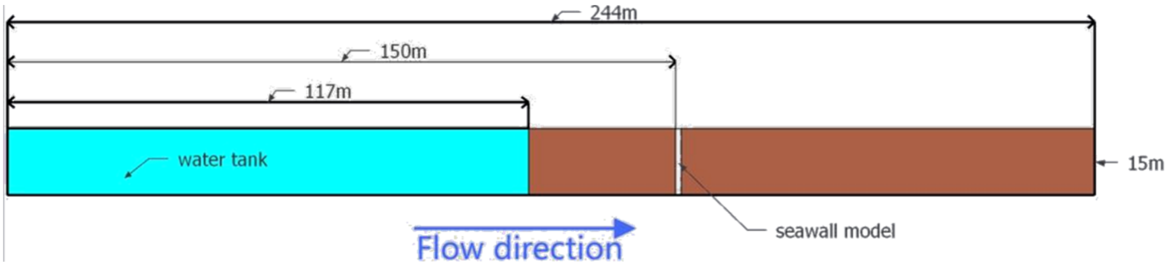

(a) top view

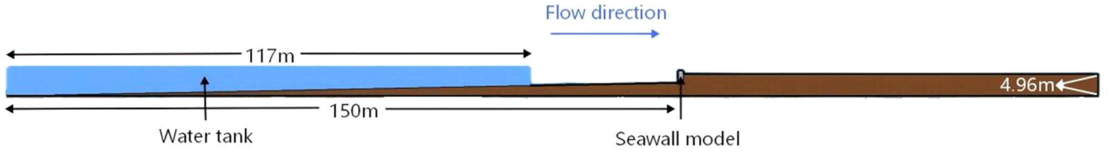

(b) side view

Figure 2. Schematic layout of the numerical wave flume, showing both the plan view and the longitudinal cross-section of the computational domain

Standard water properties were used for numerical simulations. Gravitational acceleration was set to g = -9.81 m/s^2, with the negative sign indicating that it acts in the downward vertical direction. The density ρ = 1000 kg/m^3 and the dynamic viscosity μ = 0.001 kg/m/s of water were at 20 °C, which are standard values commonly adopted in hydraulic simulations. These properties have been used in most simulations in coastal and hydraulic engineering fields and provide a standard set of laboratory conditions.

2.2.2. Seawall Models and Design Configurations

In the numerical simulations, seawall models were rigid structures positioned within the flume shown in Figure 2. The seawall has dimensions of 15 m in width, 1.25 m in thickness, and 2.8 m in height, which is representative of a low-rise coastal defense structure. A conventional solid vertical seawall served as the baseline for the modified configurations. A series of perforated vertical seawall configurations (5%, 10%, 15%, 20%, and 25%) as shown in Figure 3, was examined, with perforations distributed in accordance with established approaches by Rahman et al. [8].

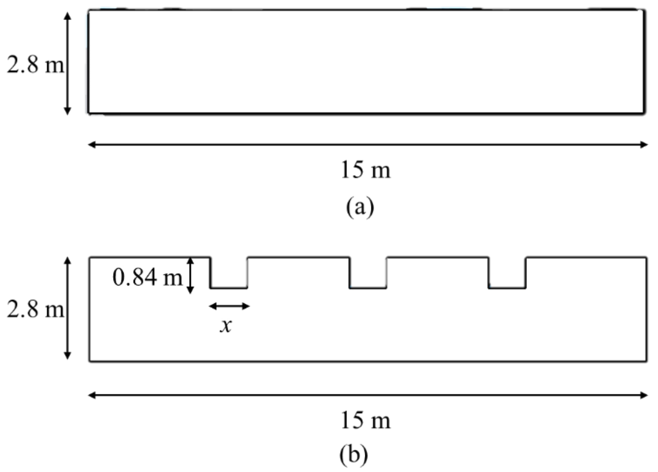

perforation ratios	x value
5%	0.25 m
10%	0.50 m
15%	0.75 m
20%	1.00 m
25%	1.25 m

Figure 3. (a) Solid and (b) perforated seawall configurations (front/back view)

To study the combined effects of perforation and crest curvature on tsunami flow, integrated perforated-recurved designs were investigated in addition to perforated vertical seawalls. This study chose two configurations of integrated perforated-recurved seawalls that were identical in all aspects except for the geometry of the recurved crest: one with a triangular recurved profile and the other with an arc recurved profile (Figure 4). In both seawall configurations, the recurved element was attached to the seaward face of the perforated seawall, so that the overall height of the seawall remained unchanged. The recurved element had a vertical height of 0.84 m and a thickness of 0.84 m, spanning the entire width of the seawall.

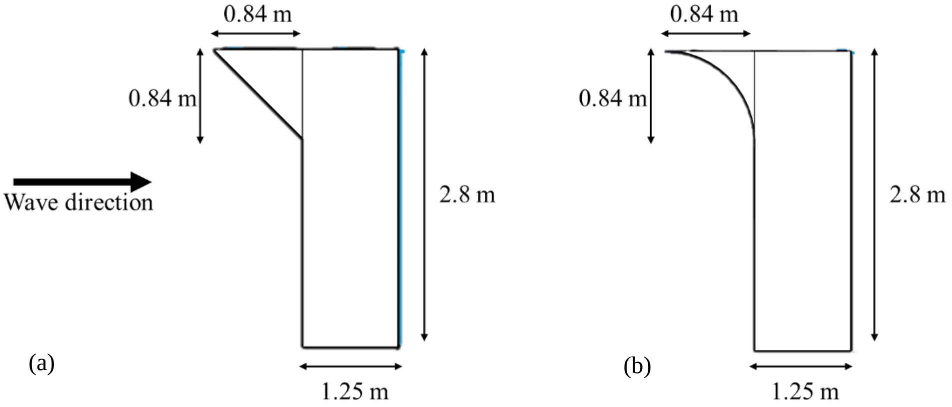

Figure 4. Recurved seawall configurations: (a) triangular recurved and (b) arc recurved

2.3. Mesh Design and Grid Resoluvtion

A series of systematic grid-refinement analyses were conducted to confirm that the numerical solutions were grid-independent. For these analyses, five progressively refined uniform grid resolutions were evaluated, with grid sizes of 0.25 m, 0.20 m, 0.15 m, 0.10 m, and 0.05 m. As the grid spacing was reduced, the changes in the measured parameters decreased, indicating that the numerical solution was converging. The Grid Convergence Index (GCI) method was adopted to measure the extent of grid refinement, as described by Celik et al. [26].

$$\text{GCI}_{\text{fine}} = F_s \frac{|\varepsilon|}{r^p - 1} \times 100\% \quad (3)$$

where the subscript "fine" indicates that the uncertainty is evaluated for the finest grid used in the study. F_s is the safety factor (taken as 1.25), r is the grid refinement rate, while p is the order of convergence. In this study, p was taken as 1, a conservative assumption, which is commonly used for complex free-surface flows where the apparent order of convergence cannot be reliably determined. The relative error ε represents the normalized difference between solutions on successive meshes and reflects the sensitivity of the numerical results to grid resolution. The GCI therefore provides a conservative estimate of the remaining discretization error in the finest-grid solution. This technique is based on Richardson Extrapolation (RE), which is widely applied in the CFD literature to provide a lower-bound estimate of the grid-spacing error in the analysis.

As mentioned previously, five grid systems consisting of 7,027,200, 13,725,000, 32,533,333, 109,800,000, and 878,400,000 computational cells were analyzed. The GCI values for each grid resolution are included in Table 1, based on the wave-induced forces acting on the 10% perforated seawall. Based on the GCI results, the solutions for mesh sizes of 0.10 m and 0.05 m exhibit similar convergence behavior. With GCI values below 7%, this implies that further mesh refinement yields only marginal improvements in solution accuracy. Thus, a mesh size of 0.10 m provides grid-independent results that accurately represent the flow while maintaining computational efficiency.

Table 1. Grid convergence index (GCI) calculation

Grid number	Grid size (m)	Fs=1.25			
		r	p	ε	GCI (%)
7,027,200	0.25		1		
13,725,000	0.2	1.25	1	0.073238	36.62
32,533,333	0.15	1.33	1	0.060727	22.77
109,800,000	0.1	1.5	1	0.025495	6.37
878,400,000	0.05	2	1	0.051824	6.48

To accurately capture complex flow patterns around the seawall, a local mesh refinement strategy was employed. As illustrated in Figure 5, a base mesh size of 0.10 m was applied throughout the majority of the computational domain (Mesh Block 1). A region of mesh refinement from 149 m to 151.5 m along the flume was implemented (Mesh Block 2), covering the seawall and its adjacent zones. This nested grid approach optimized computational efficiency and ensured detailed representation of flow separation, impact, and overtopping processes.

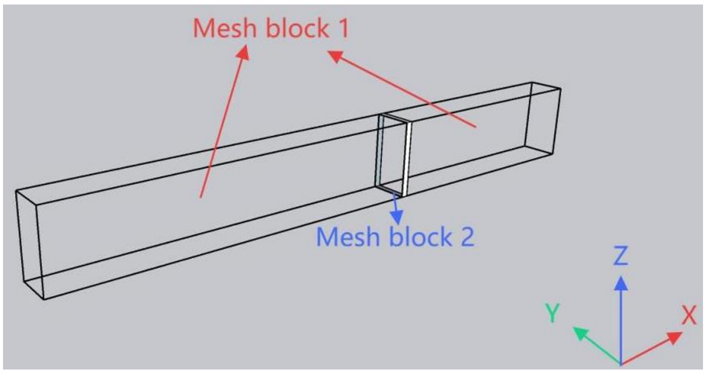

Figure 5. Mesh blocks in FLOW-3D

2.4. Experimental Validation Setup

For validation purposes, experimental tests were conducted in the Hydraulic Laboratory at UCSI University, in a wave flume 4.88 m long and 0.30 m wide (Figure 6). The flume bed was configured with a 1:50 slope to replicate coastal bathymetric conditions. A vertical reservoir gate was placed 2.34 m from the upstream end of the flume to create an impounded water column. Upon release, the generated wave formed a propagating bore that would travel down the slope.

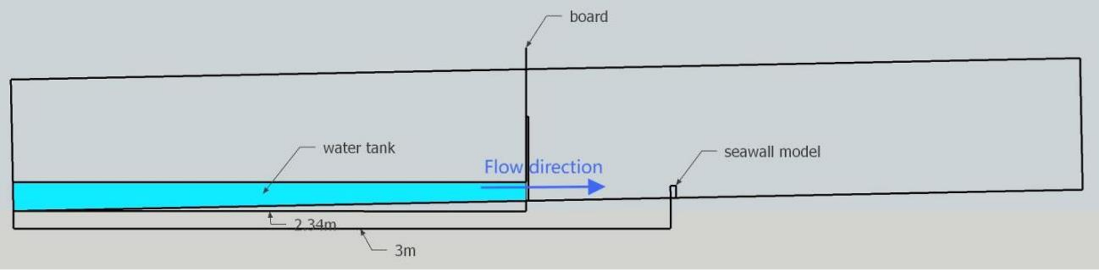

Figure 6. Schematic diagram of the experimental setup (side view)

A scaled physical model of a solid vertical seawall was employed, which is made of concrete with dimensions of 30 cm (length) x 2.5 cm (width) x 5.6 cm (height). Before installing any seawall models, free-flow experiments were conducted to assess wave dynamics in the absence of structures. After the free-flow tests, the seawall model was installed at the designated location and tested under tsunami-like waves. Side-view wave propagation, reflection, and overtopping processes were captured in the experimental setup using high-speed cameras at 60 frames per second. Spatially referenced images were then analyzed using grid markings on the flume's transparent walls to quantify these flow characteristics over the seawall.

2.5. Tsunami Wave–Seawall Simulation Scenarios

2.5.1. Perforated Seawall Configurations

For tsunami wave-seawall modelling, a numerical simulation program was developed based on combinations of initial bed conditions and impoundment depths. Moderate and near-threshold overtopping conditions were represented by selecting two impoundment depths: 4.25 m and 6.25 m. Simulations were conducted for each impoundment depth under both dry and wet bed conditions. The dry and wet bed conditions respectively represent the seaward regions with and without initial water prior to wave arrival. In the absence of a seawall, a 4.25 m impoundment generates flow depths of 2.14 m (dry bed) and 2.25 m (wet bed) at the seawall location, which are slightly below the seawall's crest, therefore representing moderate conditions with minimal overtopping. In contrast, a 6.25 m impoundment generates flow depths of 2.88 m (dry bed) and 3.04 m (wet bed), exceeding the crest elevation and resulting in severe overtopping.

For the first part, numerical simulations were conducted for a solid vertical seawall and for perforated seawalls with different perforation ratios. Notably, the free-flow (no-structure) condition was not included. Numerical repeatability was confirmed by grid-independent convergence and stable boundary conditions, so each simulation case was run only once. The selection of the optimal perforated seawall design for the subsequent studies was based on a comparative analysis of hydraulic and loading responses.

2.5.2. Integrated Perforated-Recurved Seawall Configurations

Following identification of the optimal perforated seawall configuration, two integrated perforated-recurved designs were developed by attaching recurved features (triangular and arc recurved profiles) to the seaward face of the selected perforated wall. The integrated configurations were evaluated under the same impoundment depths (4.25 m and 6.25 m) and bed conditions (dry and wet) used in Section 2.5.1. This ensured overall consistency in wave conditions and allowed direct performance comparison between the optimal perforated seawall, and the integrated perforated-recurved seawall designs.

3. Results and Discussion

3.1. Model Validation Results

All numerical results presented in this paper were obtained with the grid resolution confirmed by the mesh sensitivity analysis described in Section 2.3. The simulated waves closely matched the experimental measurements in terms of magnitude and temporal evolution (results not shown), with a relative error between the simulated and the experimental peak depths within a 10% margin. Quantitative validation was also performed using the root mean square error (RMSE) and the coefficient of determination (R^2), as summarized in Table 2. The RMSE values were 2.56 mm and 4.57 mm for the 85 mm and 125 mm cases, respectively, which correspond to relative errors below 10% when normalized by the experimental peak depth. These values fall within the acceptable range commonly reported for free-surface CFD simulations of transient hydraulic phenomena. The model's goodness of fit is further supported by high R^2 values ranging from 0.915 to 0.975 (Table 2).

Table 2. Model performance of free-flow experiments for impoundment depths of 85 mm and 125 mm

Cases	RMSE (mm)	Relative RMSE (%)	R^2
85 mm impoundment depth	2.56	5.77	0.975
125 mm impoundment depth	4.57	7.50	0.915

* Relative RMSE is defined as the RMSE normalized by the experimental peak depth.

Figure 7 presents a qualitative comparison between numerical simulations and experimental results of wave impact on a solid vertical seawall for impoundment depths of 85 mm and 125 mm. The focus of the model validation was on the major hydrodynamic parameters, including wave impact, and free-surface development. As shown in Figure 7, the experiments and simulations both captured the upward splash formation at initial impact (0.2-0.3 s), subsequent overtopping (0.4 s), and the development of landward flow behind the seawall (0.5 s). Due to limitations of the model in capturing air entrainment and experimental uncertainties arising from repeated dam-break wave generation, some discrepancies were expected. Although the experimental images captured greater irregularity in splash height and wave shape, the numerical results reproduced the overall wave evolution and the interaction sequence.

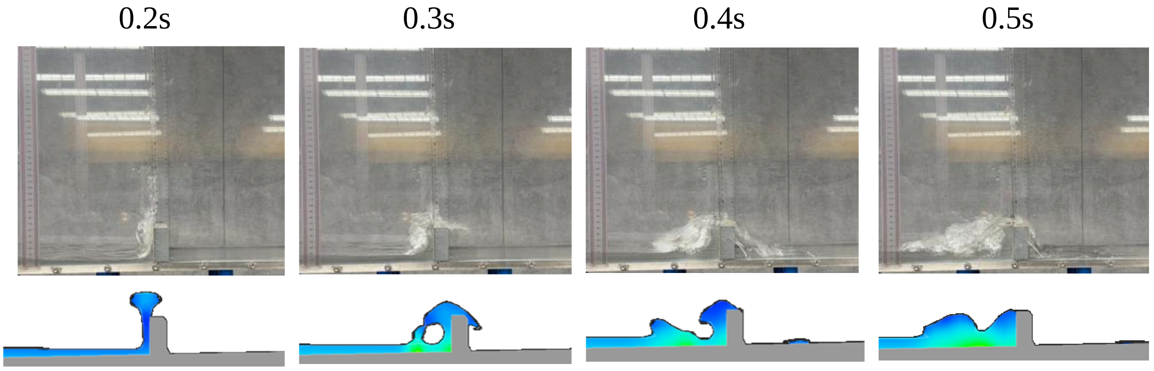

(a) 85 mm

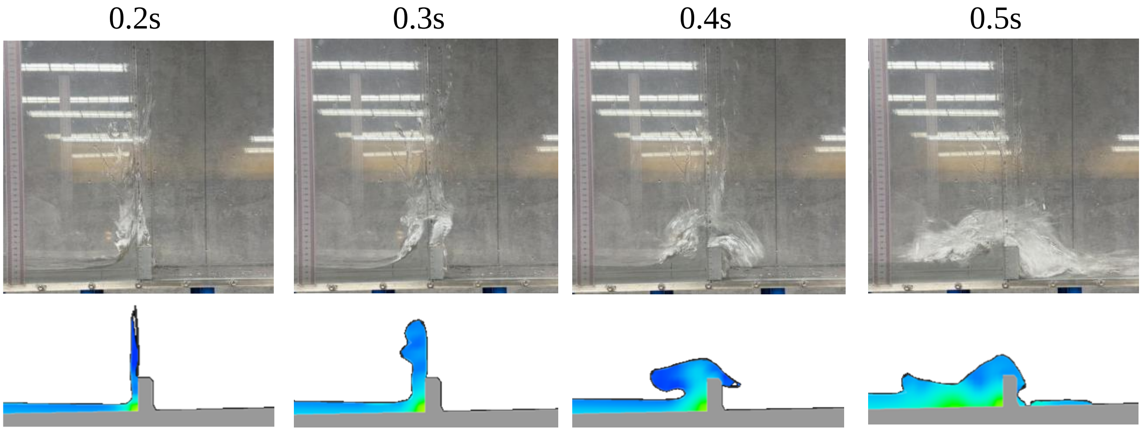

(b) 125 mm

Figure 7. Comparison of wave impact on a seawall between experimental results and numerical simulation

3.2. Hydrodynamic Flow Characteristics Near the Seawall

To assess the plausibility of the numerical predictions, Figure 8 compares the relationship between maximum flow depth and velocity obtained in this study with data reported in previous empirical studies [27-35]. As expected, larger impoundment depths produce higher maximum flow depths and velocities near the seawall location, regardless of the dry or wet bed conditions. The results of this study fall within the upper range of reported values. This behaviour reflects the extreme bore-type wave generation, and steep front conditions modelled in the present simulations.

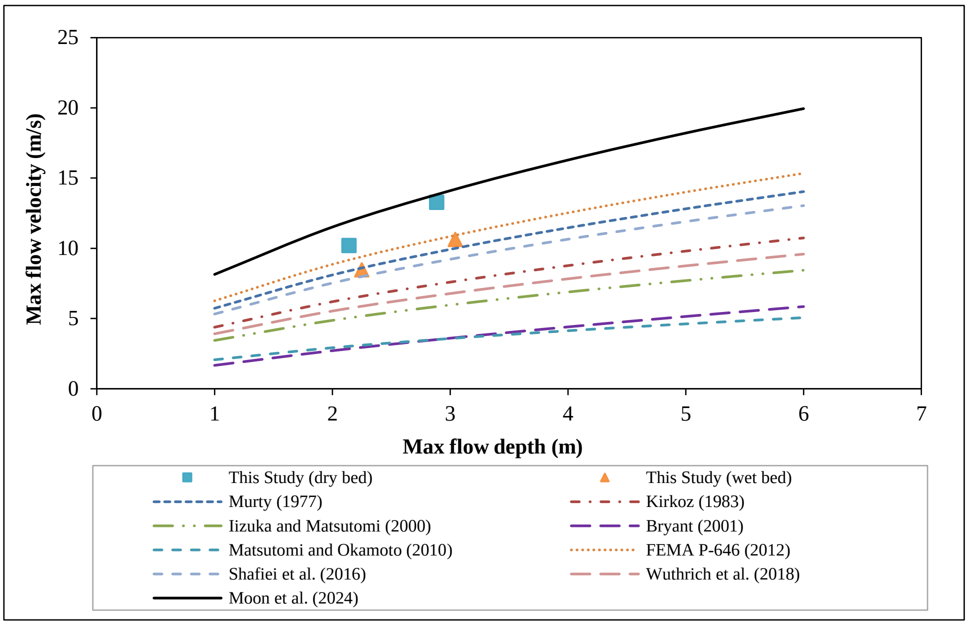

Figure 8. Maximum flow velocity corresponding to the maximum flow depth

3.3. Effects of Perforation Ratio on Tsunami-Seawall Interaction

3.3.1. Overtopping Behavior under Different Perforation Ratios

Figure 9 compares the temporal evolution of overtopping discharge for seawalls with various perforation ratios (5%, 10%, 15%, 20%, and 25%) and a solid vertical seawall for an impoundment depth of 4.25 m, under dry and wet bed conditions. Overtopping is negligible prior to wave arrival ($t < 5$ s), followed by a rapid increase associated with bore impact and run-up. Initial peak overtopping occurs between 5 and 15 s, after which the discharge reduces progressively as the wave energy dissipates. The solid seawall exhibits the lowest overtopping discharge, as the impermeable barrier restricts direct flow transmission over the crest. In contrast, perforated seawalls allow flow-through and result in higher overtopping discharges. This is consistent with the results reported by Umeda et al. [10] who show higher inland flow for perforated barriers due to reduced reflection.

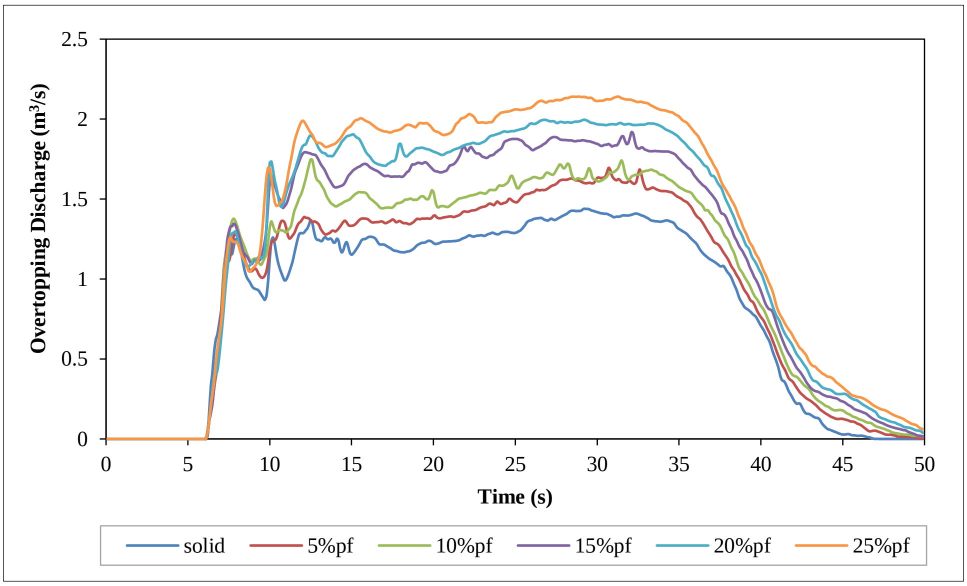

(a) Dry bed condition

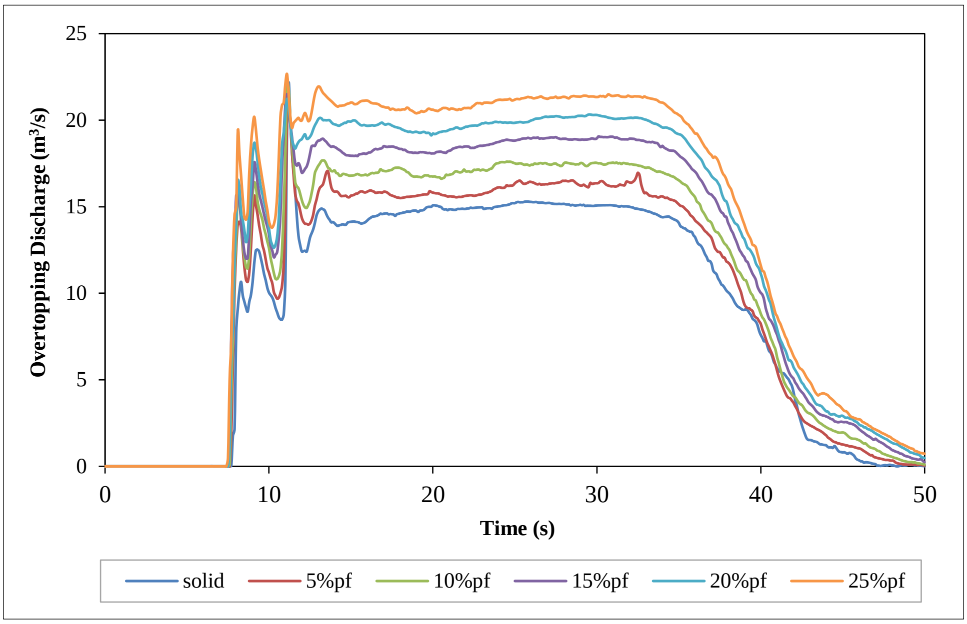

(b) Wet bed condition

Figure 9. Wave overtopping discharge comparison at different perforation ratios under 4.25 m impoundment depth

The representative wave–seawall interaction snapshots at the time of initial overtopping are presented in Figure 10, the 25% perforated seawall configuration shows a more distributed flow across the crest with less splashes and smoother overtopping jets compared with the solid seawall. This observation shows that perforation is indeed responsible for the redistribution of the overtopping flow rather than the generation of impulsive overflow. Additionally, this reflects enhanced energy dissipation due to turbulence generation and viscous effects in the perforations. While solid seawall dissipates energy primarily through reflection, perforated seawall allows a portion of incoming flow to pass through the openings, thus increasing the amount of water that reaches the crest. As a result, the overtopping discharge is expected to be higher than the solid seawall. The effect is more significant in the wet bed case, where the existing water reduces the frictional resistance and allows the flow to continue over the seawall.

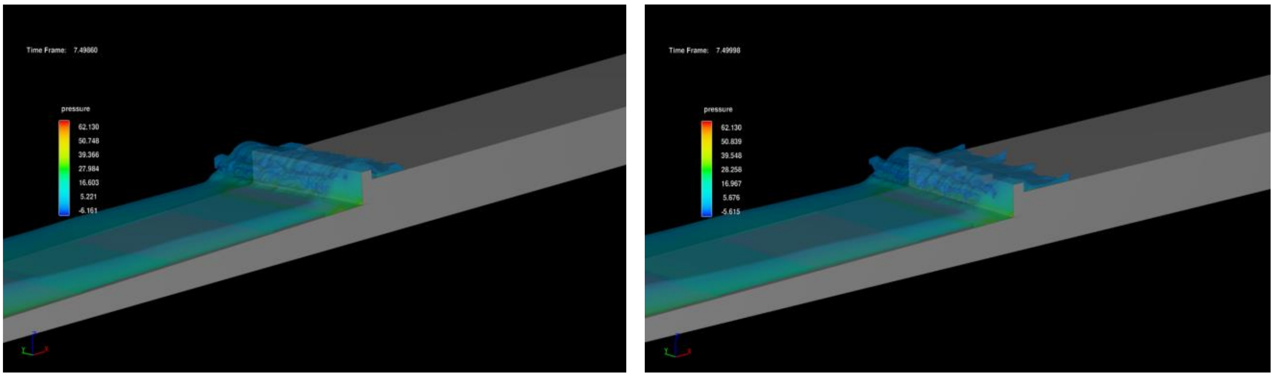

(a) (b)

Figure 10. Representative wave–seawall interaction at initial overtopping for the (a) solid and (b) 25% perforated seawall configurations under an impoundment depth of 4.25 m (wet bed condition)

In comparison to the case of lower impoundment shown in Figure 9, the overtopping initiated under near-threshold overtopping conditions occurs earlier and leads to higher discharge due to the increased wave momentum and water mass (Figure 11). Although the solid seawall still shows the lowest peak overtopping discharge, the difference between perforation configurations is less pronounced, with the incoming bore having sufficient momentum to cause overtopping, thereby diminishing the relative effect of perforation on the peak overtopping magnitude. The perforated seawalls, however, still reveal a smoother discharge with reduced short-term fluctuations, which indicates that the effect of perforation is primarily on the temporal distribution of overtopping rather than complete elimination of overtopping under extreme loading.

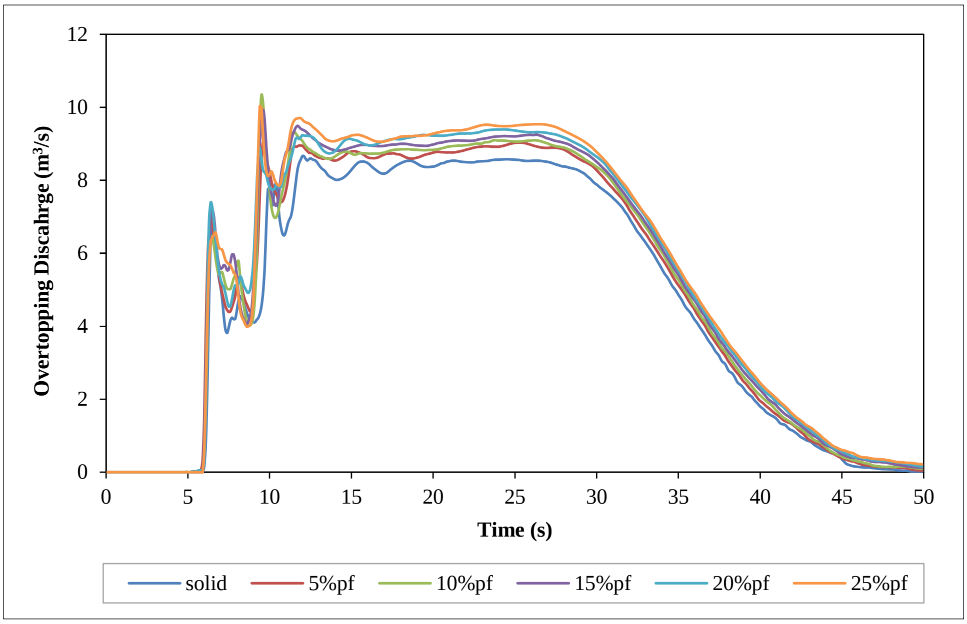

(a) Dry bed condition

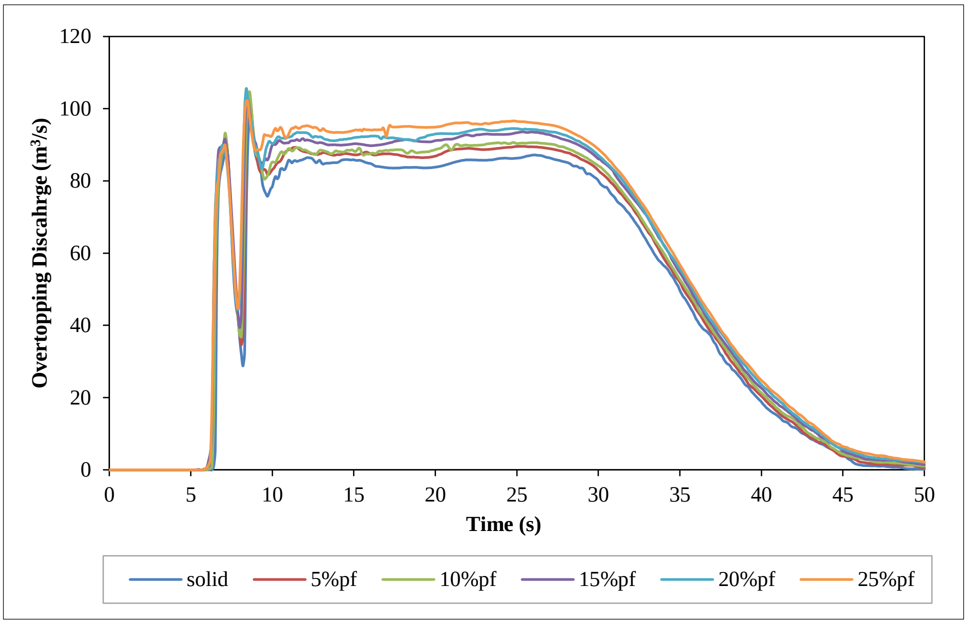

(b) Wet bed condition

Figure 11. Wave overtopping discharge comparison at different perforation ratios under 6.25 m impoundment depth

3.3.2. Horizontal Force on Seawall's Seaward Face

Figures 12 and 13 present the temporal evolution of wave-induced horizontal force acting on the seaward face of solid and perforated seawalls under various impoundment depths (4.25 m and 6.25 m) and bed conditions (dry and wet). Notably, the force time histories capture the combined effects of hydrostatic pressure, dynamic wave impact, and reflection-induced loading during tsunami bore interaction.

For an impoundment depth of 4.25 m under dry bed conditions (Figure 12-a), the solid seawall experienced the highest peak force due to strong wave reflection and concentrated impact loading. In contrast, higher perforation ratios corresponded to progressively lower peak forces. The partial-wave transmission through the perforations modifies the reflected energy at lower pressures, with reduced reflected wave energy through turbulence generation and viscous losses. In addition, flow passing through the perforations reduces the buildup of hydrostatic and hydrodynamic pressures on the seaward face, thereby reducing impulsive loading associated with wave reflection. The force time histories show greater peak reduction and a notable degree of smoothness.

For a higher impoundment depth of 6.25 m under dry-bed conditions (Figure 13-a), the same trend was observed despite the increased wave momentum and water mass exerting more forces on all seawall configurations. The observed force reduction is consistent with previous experiments by Rahman et al. [8] and Mokhtar et al. [9], who noted that force reduction was caused by loss of momentum within the perforated structures. In the present study, force reduction has been measured for a broader range of perforation ratios under both dry and wet bed tsunami conditions. Figures 12-b and 13-b show a steeper initial rise of force time histories under wet bed conditions. The initial force peak occurred earlier and occasionally reached a higher value than in dry bed conditions. This effect is thought to be caused by the presence of initial water in the seaward regions, which decreases frictional resistance and increases momentum transfer during bore impact. Subsequent to this impulsive phase, the sustained force is seen to be only slightly lower than under dry bed conditions.

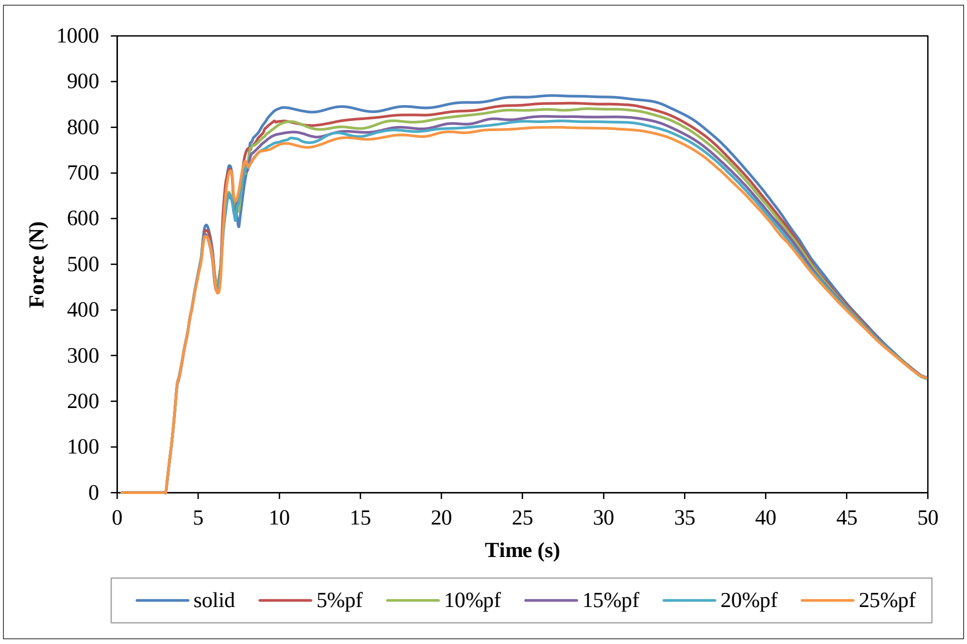

(a)

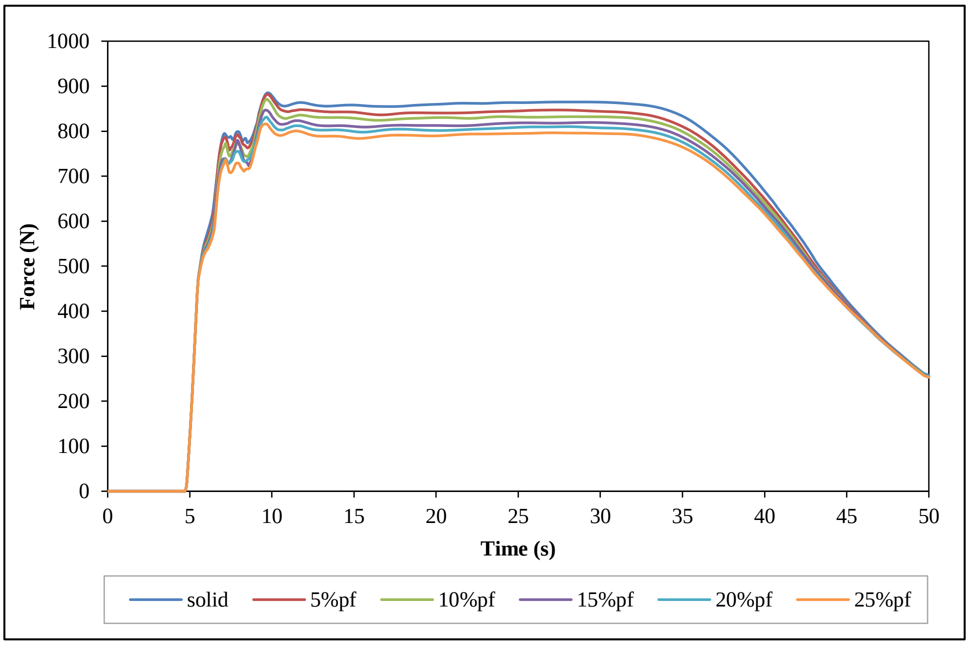

(b)

Figure 12. Time histories of horizontal wave-induced force acting on the seaward face of solid and perforated seawalls under (a) dry and (b) wet bed conditions at an impoundment depth of 4.25 m

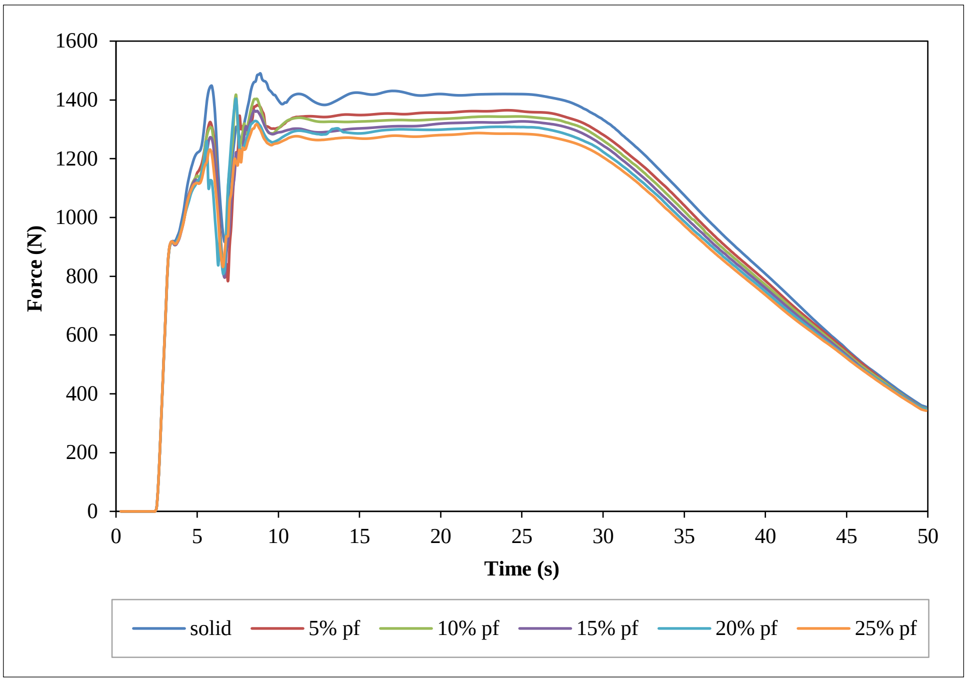

(a)

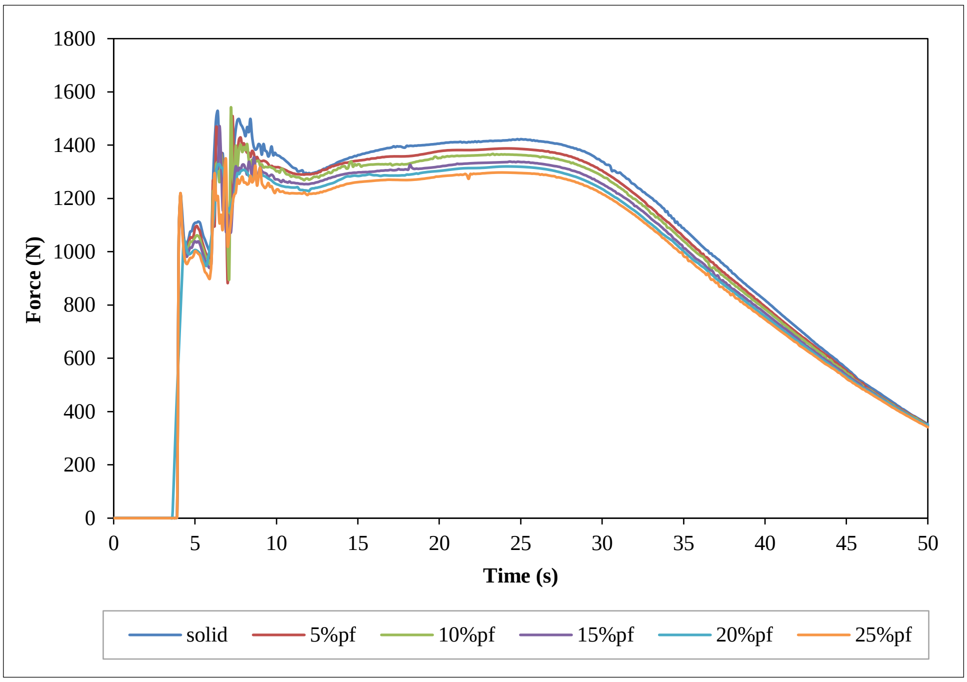

(b)

Figure 13. Time histories of horizontal wave-induced force acting on the seaward face of solid and perforated seawalls under (a) dry and (b) wet bed conditions at an impoundment depth of 6.25 m

3.3.3. Inland Inundation Characteristics

Figures 14-a and 14-b present a summary of the maximum inland flow depth and velocity measured at 50 m landward of the seawall for solid and perforated cases for impoundment depths of 4.25 m and 6.25 m, under both dry and wet bed conditions. This metric is adopted to characterize the peak inundation hazard relevant to inland flooding and structural exposure. The 50 m measurement point is considered representative of near-field inundation risk, situated immediately behind coastal defenses and within the recommended coastal setback distance in Malaysian coastal management guidelines [36].

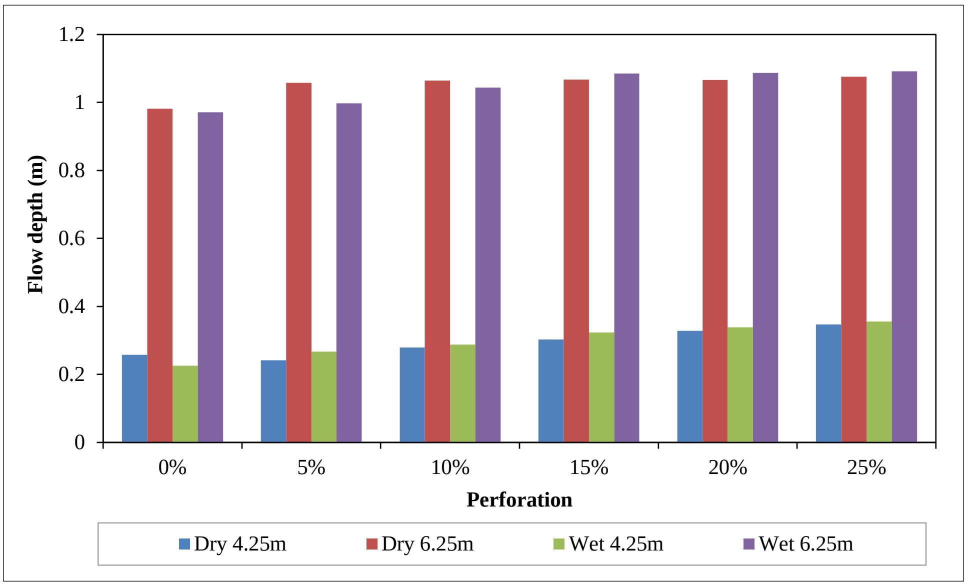

(a)

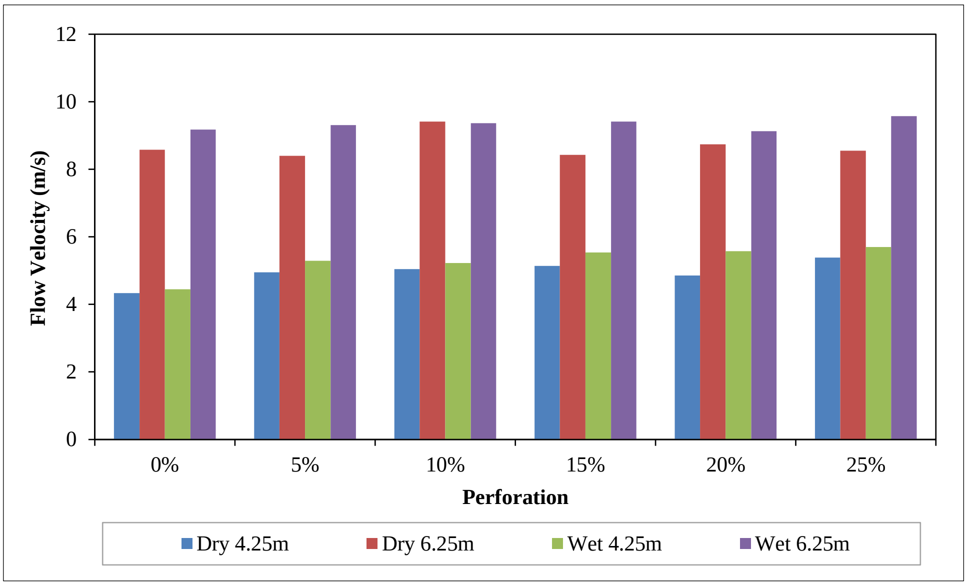

(b)

Figure 14. Maximum inland (a) flow depth and (b) velocity measured at 50 m landward of the seawall for solid and perforated configurations under dry and wet bed conditions at impoundment depths of 4.25 m and 6.25 m

For an impoundment depth of 4.25 m under dry bed conditions, the maximum inland flow depths for the perforated seawalls are slightly higher than those for the solid seawall, with peak values increasing gradually with increasing perforation ratio (Figure 14-a). This trend shows that although the perforations help in the dissipation of wave energy, they also allow a controlled amount of flow transmission inland during tsunami loading. For the larger impoundment depth of 6.25 m, the corresponding inland flow depths show a significant increase for all perforated seawall configurations, irrespective of the perforation ratio. This shows that there is a regime shift where, at high hydraulic head, the perforations are effective in lowering the reflective properties of the seawall, allowing a larger amount of water volume to flow inland. On the other hand, the maximum inland flow depths do not differ significantly across seawall configurations and perforation ratios, for both impoundment depths under wet bed conditions. In cases where the seaward zone is already inundated, the maximum inland water depth is less dependent on the flow interaction process at the seawall. Hence, the effect of perforation on the maximum inland depth is likely less pronounced under wet bed conditions.

The maximum inland velocities are presented in Figure 14-b. For the case of 4.25 m impoundment depth under dry bed conditions, a moderate increase in peak inland velocity with increasing perforation ratio is observed, which indicates the increased momentum transfer due to the perforations. For 6.25 m impoundment depth, the inland flow is dominated by the momentum of the incident wave rather than by the seawall geometry itself. The peak velocity is observed to be very high for all configurations and are not sensitive to the perforation ratio. Maximum velocity for wet bed conditions is always the highest for all cases, and it varies insignificantly with perforation ratio. This is consistent with the observation that bed condition and impoundment depth are the dominant factors governing inland flow velocity, with the perforation ratio playing a secondary role.

Overall, the results for force, overtopping, and inland flow indicate that perforation does not eliminate wave energy but rather redistributes it between structural loading and inland flow. Unlike solid seawalls, perforated seawalls allow continuous flow penetration. With the increase in the perforation ratio, the transmitted discharge and inland flow increase, while the reflected wave energy and peak forces decrease. From the practical perspective, this means that an improvement in structural resilience may come at the cost of an increase in inland inundations hazards. While the reduction of impulsive forces lowers the risk of structural failure, the resulting increase in overtopping can pose significant threats to human safety in the protected hinterland, especially in the densely populated coastal zones. Therefore, perforation cannot be assessed solely on the basis of structural performance. This trade-off highlights the need to balance the structural force reduction with the potential increase in inland hazards, as discussed in Section 3.4.

3.4. Performance Evaluation and Optimization of Perforated Seawall Designs

To enable a systematic comparison of hydraulic performance among different perforation ratios, a multi-criteria scoring approach was adopted. Four key performance metrics were considered, namely: (i) wave-induced force acting on the seaward face of the seawall, (ii) inland flow depth, (iii) inland flow velocity, and (iv) total overtopping volume. For each metric, the six seawall configurations (solid and 5%, 10%, 15%, 20%, and 25% perforation ratios) were ranked from best to worst, with a score of 1 assigned to the top-performing case and 6 to the worst. Table 3 summarizes the scoring results under four wave scenarios, comprising: dry and wet bed conditions with impoundment depths of 4.25 m and 6.25 m. Lower total scores therefore indicate better overall hydraulic performance.

Table 3. Ranking scores for hydraulic performance indicators

		Solid	**5%**	**10%**	**15%**	**20%**	**25%**
Dry 4.25 m	Force	3	6	5	4	2	1
	Inland Water depth	2	1	3	4	5	6
	Inland Flow Velocity	1	3	4	5	2	6
	Overtopping Volume	1	2	3	4	5	6
Dry 6.25 m	Force	2	6	4	5	1	3
	Water depth	1	2	3	5	4	6
	Velocity	4	1	6	2	5	3
	Overtopping Volume	1	2	3	4	5	6
Wet 4.25 m	Force	5	6	4	2	1	3
	Water depth	5	1	2	3	4	6
	Velocity	1	3	2	4	5	6
	Overtopping Volume	1	2	3	4	5	6
Wet 6.25 m	Force	4	3	5	2	6	1
	Water depth	1	2	3	4	5	6
	Velocity	2	3	4	5	1	6
	Overtopping Volume	1	2	3	4	5	6
	Total score	**35**	**45**	**57**	**61**	**61**	**77**

* Rank 1 indicates best performance; rank 6 indicates worst

When the total scores are summed across all wave scenarios, the 5% perforated seawall shows the best overall hydraulic performance, achieving the lowest cumulative score among the perforated configurations. Perforation ratios in the range of 10–20% exhibit decreasing sensitivity in hydraulic response, with scores ranging from 57 to 64 within this intermediate range. However, a further increase to 25% perforation results in a substantial reduction in performance, particularly in terms of overtopping volume and inland hydraulic response.

To assess the trade-off between savings on construction materials and hydraulic performance, two indices were created. The Performance Loss Index (PLI) assesses the relative increase in total score compared to the solid seawall. The Material Efficiency Index (MEI) correlates performance loss to material savings. High MEI values suggest a favorable outcome between hydraulic performance loss and material efficiency.

$$\mathrm{PLI} = \frac{S_{\mathrm{perforation}} - S_{\mathrm{solid}}}{S_{\mathrm{solid}}} \tag{4}$$

$$\mathrm{MEI} = \frac{\text{Material Saving Ratio (MSR)}}{\text{Performance Loss Index (PLI)}} \tag{5}$$

Table 4 shows the results for indices of performance loss and material efficiency. The 5% perforated seawall has the best overall hydraulic performance, but its modest material savings yield a low MEI. In contrast, a high degree of perforation results in significant performance loss and a poor efficiency index. The 20% perforation ratio provides the most balanced compromise between hydraulic performance loss and material efficiency (highest MEI). This balanced configuration is therefore more suitable for integrated geometric enhancement.

Table 4. Performance loss and material efficiency indices

Perforation Ratio	Material Saving Ratio (MSR)	PLI	MEI
Solid (0%)	0	0	–
5%	0.015	0.286	0.0525
10%	0.030	0.629	0.0478
15%	0.045	0.743	0.0606
20%	0.060	0.743	0.0808
25%	0.075	1.200	0.0630

3.5. Performance Enhancement Using Integrated Perforated-Recurved Seawall

The results presented in Sections 3.3 and 3.4 indicate that perforation-based mitigation is most effective under near-threshold overtopping conditions, particularly for an impoundment depth of 6.25 m. However, its relative effectiveness diminishes under wet bed conditions. Two integrated perforated–recurved seawall configurations were investigated by attaching recurved crest elements to the seaward face of the optimal perforated seawall (20% perforation). Figure 15 presents representative snapshots of wave–seawall interaction for an impoundment depth of 6.25 m under dry-bed conditions. Sequential snapshots at 4.0 s, 4.5 s, 5.0 s, 5.5 s and 6.0 s illustrate the initial wave impact, splash-up, overtopping initiation, wave collapse, and landward inundation, respectively.

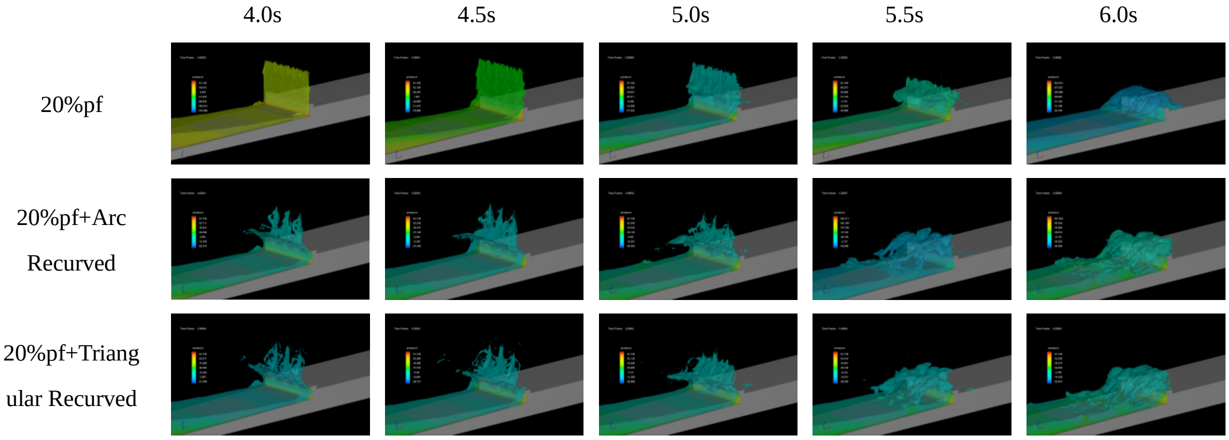

Figure 15. Representative wave–seawall interaction snapshots illustrating qualitative differences between configurations for an impoundment depth of 6.25 m (dry bed)

According to Figure 15, the addition of a recurved crest alters the wave–structure interactions by redirecting the incoming bore upward and seaward. This is consistent with studies on recurved parapets by Dong et al. [18], showing that crest deflection can significantly reduce overtopping. While perforation alone reduces horizontal forces at the cost of increasing overtopping and inland flow, the perforated–recurved design decreases direct wave transmission over the crest while preserving the damping effects associated with perforation. Even with the equivalent overall crest height, the integrated designs demonstrate a delayed overtopping onset and lower peak discharge as compared to the perforated-only seawall (Figure 15). Consequently, the inland flow depth and velocity are lower than in the perforated-only case.

The energy dissipation was compared between the 20% perforated and integrated perforated–recurved seawall configurations in Figure 16. For a specific bed condition and impoundment depth, the energy of the incoming waves was the same for all configurations. Incident energy was also determined by integrating the energy flux across all configurations over a consistent 2.5-s time window to capture the dominant incident wave and disregard reflected waves. Energy associated with overtopping was calculated by integrating the energy flux inland after the wave arrived using time windows aligned with the incident energy phases.

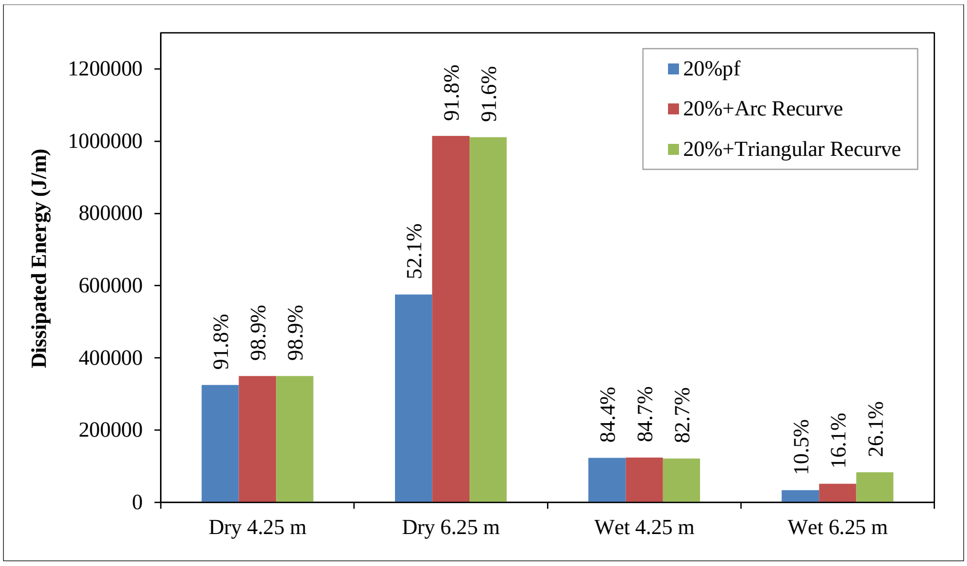

Figure 16. Energy dissipation for 20% perforated and integrated perforated–recurved seawall configurations

For moderate or weak overtopping conditions (4.25 m), the impact of the recurved crest is even less pronounced for both dry and wet bed conditions. In these wave scenarios, perforation alone provides sufficient energy dissipation, and the extra geometric modification provides only marginal energy dissipation improvements. For near-threshold overtopping conditions (6.25 m), the addition of recurved crest elements increases energy dissipation compared to the perforated-only configuration, as both recurved configurations increased energy dissipation from approximately 52% for the perforated-only seawall to over 91% under dry bed conditions (Figure 16).

For wet bed conditions at 6.25 m, energy dissipation remains consistently the lowest across all configurations due to pre-existing water that limits pressure gradients and reduces turbulence generation. However, the integrated perforated–recurved seawalls still outperformed the perforated-only configuration. Notably, the triangular recurved profile achieves higher energy dissipation (26%) than the arc recurved profile (16%). These results suggest that a sharper geometric deflection is more effective under wet bed, near-threshold overtopping conditions, likely due to sharper flow separation and more efficient jet redirection compared to smoother arc profile.

4. Conclusions

This study investigated hydraulic performance of solid vertical, perforated, and integrated perforated–recurved seawall designs under various tsunami wave scenarios, with particular emphasis on wave-induced forces, overtopping, inland inundation, and energy dissipation. Based on the results, the main findings are summarized as follows:

- Perforation significantly reduces wave-induced horizontal forces by approximately 25-30% compared with a solid vertical seawall through momentum transmission and turbulence within the openings. However, this force reduction is accompanied by an increase in overtopping discharge and inland flow depth and velocity. This leads to a trade-off evaluation between structural load reduction and inland flood hazard using the Material Efficiency Index (MEI). Based on the MEI calculation, there is an optimal perforation ratio of 20% that offers a better compromise between the loss of hydraulic performance and material efficiency. Higher perforation ratios result in greater force reduction but with a considerable increase in inland inundation.
- The incorporation of recurved crest elements improves hydraulic performance by redirecting uprushing flow seaward and reducing overtopping. The integrated perforated–recurved seawalls showed significantly higher energy dissipation values than perforated-only seawalls, with an overall increase from approximately 52% to over 90% under dry bed near-threshold overtopping. In the perforated-recurved seawalls, triangular recurved profiles performed marginally better than arc profiles, especially for wet bed, near-threshold overtopping conditions, which is attributed to better flow separation and redirection.

In conclusion, this staged evaluation framework, progressing from perforation optimization to geometric enhancement, demonstrates that the integrated perforated and recurved seawall concept can partly mitigate the disadvantages of each design and provides a rational and effective method for enhancing the resilience of seawalls against tsunami loading. In a broader context, these findings contribute to sustainable coastal flood risk reduction strategies by promoting resilient coastal protection infrastructure that balances structural safety of seawalls, inland hazard mitigation, and material efficiency. The current analysis is based on three-dimensional CFD simulations. While the model was validated with laboratory experiments, actual coastal conditions, such as complex bathymetry, sediment transport, and nonlinear wave processes, cannot be fully represented. Therefore, the applicability of these findings should be interpreted in light of these limitations, and future studies incorporating site-specific conditions are recommended.

5. Declarations

5.1. Author Contributions

Conceptualization, W.J. and W.C.M.; methodology, W.J. and W.C.M.; software, W.J.; validation, W.J.; formal analysis, W.J. and W.C.M.; investigation, W.J.; data curation, W.J.; writing—original draft preparation, W.J.; writing—review and editing, W.C.M. and H.T.P.; supervision, W.C.M., H.D., and T.L.L.; funding acquisition, W.C.M. and J.C.L. All authors have read and agreed to the published version of the manuscript.

5.2. Data Availability Statement

The data presented in this study are available on request from the corresponding author.

5.3. Funding

This work was supported by the Ministry of Higher Education of Malaysia, through Fundamental Research Grant Scheme (FRGS) [FRGS/1/2024/TK06/UCSI/02/1].

5.4. Acknowledgments

The authors gratefully acknowledge the support provided through the Zhejiang–Malaysia Joint Laboratory on Marine Low-Carbon (Green) Building Materials, within whose framework the experimental seawall model and related research activities were conducted.

5.5. Conflicts of Interest

The authors declare no conflict of interest.

6. References

[1] Sugawara, D. (2020). Trigger mechanisms and hydrodynamics of tsunamis. Geological Records of Tsunamis and Other Extreme Waves, 47–73. doi:10.1016/B978-0-12-815686-5.00004-3.

[2] McGovern, D. J., Allsop, W., Rossetto, T., & Chandler, I. (2023). Large-scale experiments on tsunami inundation and overtopping forces at vertical sea walls. Coastal Engineering, 179, 104222. doi:10.1016/j.coastaleng.2022.104222.

[3] Satake, K. (2012). The 2011 Tohoku, Japan, earthquake and tsunami. Extreme Natural Hazards, Disaster Risks and Societal Implications, 1, 310–321. doi:10.1017/CBO9781139523905.031.

[4] Telford, J., Cosgrave, J., & Houghton, R. (2006). Joint evaluation of the international response to the Indian Ocean tsunami. Synthesis Report: Tsunami Evaluation Coalition (TEC), 1-191.

[5] Al-Mansob, R. A. E. A., Hoong, O. M., Azahar, W. N. A. W., Ng, J. L., Alsharef, J. M. A., & Ali, S. I. A. (2021). The effect of carbon-nanofiber and hydrated lime on weak soil stability. Malaysian Construction Research Journal, 14(Special Issue 3), 1–11.

[6] Suppasri, A., Shuto, N., Imamura, F., Koshimura, S., Mas, E., & Yalciner, A. C. (2013). Lessons Learned from the 2011 Great East Japan Tsunami: Performance of Tsunami Countermeasures, Coastal Buildings, and Tsunami Evacuation in Japan. Pure and Applied Geophysics, 170(6–8), 993–1018. doi:10.1007/s00024-012-0511-7.

[7] Paulik, R., Gusman, A., Williams, J. H., Pratama, G. M., Lin, S. Lin, Prawirabhakti, A., Sulendra, K., Zachari, M. Y., Fortuna, Z. E. D., Layuk, N. B. P., & Suwarni, N. W. I. (2019). Tsunami Hazard and Built Environment Damage Observations from Palu City after the September 28 2018 Sulawesi Earthquake and Tsunami. Pure and Applied Geophysics, 176(8), 3305–3321. doi:10.1007/s00024-019-02254-9.

[8] Rahman, S., Akib, S., Khan, M. T. R., & Shirazi, S. M. (2014). Experimental study on tsunami risk reduction on coastal building fronted by sea wall. The Scientific World Journal, 2014(1), 729357. doi:10.1155/2014/729357.

[9] Mokhtar, Z. A., Mohammed, T. A., Yusuf, B., & Lau, T. L. (2019). Experimental investigation of tsunami bore impact pressure on a perforated seawall. Applied Ocean Research, 84, 291–301. doi:10.1016/j.apor.2018.12.015.

[10] Umeda, S., Saitoh, T., & Furumichi, H. (2018). Mitigation effects of onshore-perforated barriers on inundation and forces induced by tsunami and tsunami-driven objects. Ocean Engineering, 152, 89–99. doi:10.1016/j.oceaneng.2018.01.051.

[11] Van Dang, H., Park, H., Lee, D., Shin, S., Lee, E., Cox, D., & Lomonaco, P. (2022). Physical Modeling of Hard Structure Effects on Tsunami Force Reduction in Urban Coastal Environment. Ports 2022: Port Engineering - Papers from Sessions of the 16th Triennial International Conference, 1, 417–427. doi:10.1061/9780784484395.042.

[12] Halvorson, B., & Huang, Z. (2024). Study of effects of perforation layouts on wave energy dissipation caused by a submerged perforated breakwater in front of a vertical seawall. Ocean Engineering, 311, 119025. doi:10.1016/j.oceaneng.2024.119025.

[13] Shafaei, H., Esmaili, K., & Beheshti, A. A. (2025). Experimental assessment of the effect of porous groin on flow hydrodynamics in a meandering compound channel. Advances in Water Resources, 206, 105137. doi:10.1016/j.advwatres.2025.105137.

[14] Gupta, A., Behera, M. R., & Heidarpour, A. (2019). Numerical modelling of hydrodynamic impact of tsunami on coastal structures in the presence of curved sea wall. Lecture Notes in Civil Engineering, 22, 547–558. doi:10.1007/978-981-13-3119-0_33.

[15] Ravindar, R., Sriram, V., & Salauddin, M. (2022). Numerical modelling of breaking wave impact loads on a vertical seawall retrofitted with different geometrical configurations of recurve parapets. Journal of Water and Climate Change, 13(10), 3644–3674. doi:10.2166/wcc.2022.211.

[16] Ghassemizadeh, S. M., & Ketabdari, M. J. (2022). Modeling of Solitary Wave Interaction with Curved Face Seawalls Using Numerical Method. Advances in Civil Engineering, 2022(1), 5649637. doi:10.1155/2022/5649637.

[17] Ghassemizadeh, S. M., ShojaeeBaghdar, F., Mazaherizaveh, A., ShojaeeBaghdar, R., Ghasemizadeh, A., & Talesh-Alikhani, E. (2026). Numerical Comparison of Solitary Wave Interactions with Concave, Convex, and Sloped Seawalls: Hydrodynamics, Loads, and Turbulence. Water Waves, 1–34. doi:10.1007/s42286-026-00131-2.

[18] Dong, S., Salauddin, M., Abolfathi, S., & Pearson, J. (2021). Wave impact loads on vertical seawalls: Effects of the geometrical properties of recurve retrofitting. Water (Switzerland), 13(20), 2849. doi:10.3390/w13202849.

[19] Harish, S., Sriram, V., Schüttrumpf, H., & Sannasiraj, S. A. (2022). Tsunami-like Flow-Induced Forces on the Landward Structure behind a Vertical Seawall with and without Recurve Using OpenFOAM. Water (Switzerland), 14(13), 1986. doi:10.3390/w14131986.

[20] Benoit, M., Benguigui, W., Teles, M., Robaux, F., & Peyrard, C. (2023). Two-phase CFD simulation of breaking waves impacting a coastal vertical wall with a recurved parapet. International Journal of Offshore and Polar Engineering, 33(2), 123–131. doi:10.17736/ijope.2023.sv03.

[21] de Almeida, E. (2025). Design considerations for coastal structures subject to confined wave impacts. Australasian Coasts and Ports 2025 Conference: Adelaide: Engineers Australia, 284–290.

[22] Gísladóttir, L. M., Castellino, M., Dermentzoglou, D., Hendriks, M. A. N., de Girolamo, P., van Gent, M. R. A., & Antonini, A. (2025). Curved concrete crownwalls on vertical breakwaters under impulsive wave load: Finite Element Analysis. Coastal Engineering, 201, 104791. doi:10.1016/j.coastaleng.2025.104791.

[23] Yakhot, V., & Orszag, S. A. (1986). Renormalization group analysis of turbulence. I. Basic theory. Journal of Scientific Computing, 1(1), 3–51. doi:10.1007/BF01061452.

[24] Hirt, C. W., & Nichols, B. D. (1981). Volume of fluid (VOF) method for the dynamics of free boundaries. Journal of Computational Physics, 39(1), 201–225. doi:10.1016/0021-9991(81)90145-5.

[25] Hirt, C. W., & Sicilian, J. M. (1985). Porosity Technique for the Definition of Obstacles in Rectangular Cell Meshes. Proceedings of the 4th International Conference on Ship Hydrodynamics, 450–468.

[26] Celik, I. B., Ghia, U., Roache, P. J., Freitas, C. J., Coleman, H., & Raad, P. E. (2008). Procedure for estimation and reporting of uncertainty due to discretization in CFD applications. Journal of Fluids Engineering, Transactions of the ASME, 130(7), 0780011–0780014. doi:10.1115/1.2960953.

[27] Murty, T. S. (1977). Seismic sea waves: Tsunamis. Department of Fisheries and the Environment, Fisheries and Marine Service, Ottawa, Canada.

[28] Kirkgöz, M. S. (1983). Breaking and Run-up of Long Waves. Tsunamis: Their Science and Engineering, 467–478. doi:10.1007/978-94-009-7172-1_35.

[29] Iizuka, H., & Matsutomi, H. (2000). Damage due to the flooding flow of tsunami. Proceedings of Coastal Engineering, JSCE, 47, 381–385.

[30] Bryant, E. (2008). Tsunami: the underrated hazard. Berlin, Heidelberg: Springer, Berlin, Germany. doi:10.1007/978-3-540-74274-6_5.

[31] Matsutomi, H., & Okamoto, K. (2010). Inundation flow velocity of tsunami on land. Island Arc, 19(3), 443–457. doi:10.1111/j.1440-1738.2010.00725.x.

[32] FEMA P-646. (2012). Guidelines for design of structures for vertical evacuation from tsunamis. Federal Emergency Management Agency (FEMA), Washington, D.C., United States.

[33] Shafiei, S., Melville, B. W., & Shamseldin, A. Y. (2016). Experimental investigation of tsunami bore impact force and pressure on a square prism. Coastal Engineering, 110, 1–16. doi:10.1016/j.coastaleng.2015.12.006.

[34] Wüthrich, D., Pfister, M., Nistor, I., & Schleiss, A. J. (2018). Experimental study of tsunami-like waves generated with a vertical release technique on dry and wet beds. Journal of Waterway, Port, Coastal, and Ocean Engineering, 144(4), 04018006. doi:10.1061/(ASCE)WW.1943-5460.0000447.

[35] Moon, W. C., Lau, T. L., & Puay, H. T. (2024). Insights into the flow characteristics of tsunami boreand surges: a case study of Malaysian coastline. Ocean and Coastal Research, 72, 24067. doi:10.1590/2675-2824072.23200.

[36] D.I.D. Manual. (2008). Coastal Management: Volume 3. Department of Irrigation and Drainage (D.I.D.), Government of Malaysia, Kuala Lumpur, Malaysia.